Rethinking Diffusion Model-Based Video Super-Resolution: Leveraging Dense Guidance from Aligned Features

Jingyi Xu^{12*}

Meisong Zheng^{2*}

Ying Chen² Mai Xu¹

Minglang Qiao¹

Xin Deng¹

¹Department of Electronic and Information Engineering, Beihang University ²Department of Tao Technology, Alibaba Group

Corresponding author: Ying Chen yingchen@alibaba-inc.com, Xin Deng cindydeng@buaa.edu.cn *These authors contributed equality to this work

ABSTRACT

Diffusion model (DM) based Video Super-Resolution (VSR) approaches achieve impressive perceptual quality. However, they suffer from error accumulation, spatial artifacts, and a trade-off between perceptual quality and fidelity, primarily caused by inaccurate alignment and insufficient compensation between video frames. In this paper, within the DM-based VSR pipeline, we revisit the role of alignment and compensation between adjacent video frames and reveal two crucial observations: (a) the feature domain is better suited than the pixel domain for information compensation due to its stronger spatial and temporal correlations, and (b) warping at an upscaled resolution better preserves high-frequency information, but this benefit is not necessarily monotonic. Therefore, we propose a novel Densely Guided diffusion model with Aligned Features for Video Super-Resolution (DGAF-VSR), with an Optical Guided Warping Module (OGWM) to maintain high-frequency details in the aligned features and a Feature-wise Temporal Condition Module (FTCM) to deliver dense guidance in the feature domain. Extensive experiments on synthetic and real-world datasets demonstrate that DGAF-VSR surpasses state-of-the-art methods in key aspects of VSR, including perceptual quality (35.82% DISTS reduction), fidelity (0.20 dB PSNR gain), and temporal consistency (30.37% tLPIPS reduction).

1 Introduction

Video Super-Resolution (VSR) has gained significant attention due to the increasing demand for high-quality videos. Unlike single-image super-resolution (SISR) techniques, VSR leverages temporal information from adjacent frames, which are highly correlated but spatially misaligned, to enhance both spatial detail recovery and temporal consistency. Traditional VSR approaches predominantly rely on handcrafted alignment and fusion mechanisms to compensate for inter-frame motion [1, 2, 3, 4]. However, these methods suffer from limited feature extraction and alignment capabilities, inevitably leading to high-frequency information loss and reconstruction artifacts. To overcome these limitations, deep learning-based VSR methods have advanced rapidly in recent years [5, 6, 7, 8]. These approaches focus on reconstructing high-frequency details of each frame by leveraging adjacent frames through various deep neural networks. Specifically, Chan et al. [5] propose a streamlined VSR pipeline that incorporates bidirectional propagation, optical flow-based alignment, feature aggregation, and upsampling operations. This framework has been widely adopted in subsequent VSR networks [9, 10, 11]. Despite achieving promising fidelity, these methods often produce inferior perceptual results, such as blurring and over-smoothing.

Recent breakthroughs in generative models offer new avenues for addressing this issue. In particular, diffusion model (DM) based VSR methods [12, 13, 14] demonstrate remarkable effectiveness in generating high-resolution videos with excellent perceptual quality and maintain temporal consistency. For instance, Zhou *et al.* [12] integrate temporal layers with

flow-guided propagation in a diffusion model for maintaining temporal coherence. Rota *et al.* [13] introduce the temporal conditioning module into a pre-trained diffusion model to enhance video stability. However, these approaches enhance perceptual quality at the expense of limited fidelity. Additionally, they suffer from error accumulation due to inaccurate feature alignment.

To resolve the above challenges, in this paper, a Densely Guided diffusion model with Aligned Features for Video Super-Resolution (DGAF-VSR) is proposed. DGAF-VSR consists of a Flow prediction Module (FM) for bidirectional optical flow estimation, diffusion steps for guided feature generation, and a pre-trained VAE decoder for high-resolution (HR) frame reconstruction. Each diffusion step integrates two key modules: the Optical Guided Warping Module (OGWM) and the Featurewise Temporal Condition Module (FTCM). Notably, both the OGWM and FTCM modules are designed based on two key observations regarding effective feature alignment and guidance: the origin of feature guidance's effectiveness and the effect of rescaling-based warping on high-frequency feature preservation. The OGWM module enables accurate feature alignment while preserving high-frequency details for richer textures. The FTCM module facilitates fine-grained information integration from aligned adjacent features through dense feature guidance. Due to its stronger spatial and temporal correlations, the DGAF-VSR can effectively leverage information from current and adjacent frames to ensure fidelity and high-frequency reconstruction. Comprehensive experiments on diverse synthetic and real-world datasets demonstrate that DGAF-VSR achieves state-of-the-art performance in terms of perceptual quality, fidelity, and temporal consistency.

The main contributions of this paper are summarized as follows:

- We quantitatively analyze the source of feature guidance's effectiveness, and the impact of rescaling and warping on high-frequency feature information, in diffusion-based VSR pipelines. These two observations motivate the design of our OGWM and FTCM.
- OGWM effectively reduces cumulative errors through a straightforward rescaling-based warping strategy, which enables accurate feature alignment.
- FTCM effectively bridges the gap between perceptual quality and fidelity through dense guidance strategy, which preserves the original video information during the diffusion process.

2 Related works

2.1 Video Super-Resolution Networks

Convolutional neural networks (CNNs) have dominated VSR due to their efficient local feature extraction capability [15, 16, 8, 5, 9, 7]. Cao *et al.* [17] pioneer the adaptation of transformer architectures for VSR through their temporal mutual attention mechanism, and subsequent methods [18, 6, 19] further advance Cao *et al.* through improved modeling of global spatial and temporal dependencies. While these approaches achieve superior fidelity, they often produce inferior perceptual results, primarily manifested as blurring and over-smoothing. To solve these problems, RealBasicVSR [10] employs various degradation strategies to synthesize training data and utilizes perceptual loss to improve perceptual quality. VideoGigaGAN [20] leverages the rich generative prior from GigaGAN [21] to produce super-resolution videos with high-frequency details.

Diffusion models (DMs) have demonstrated superior versatility in image generation compared to generative adversarial networks (GANs). In the context of SISR, diffusion model (DM)-based methods [22, 23, 24, 25, 26] consistently achieve enhanced perceptual quality and photorealistic textural details. However, existing DM-based VSR methods face two critical challenges: (a) Their inherent stochasticity exacerbates temporal flickering artifacts across video frames, and (b) their training pipelines require prohibitively high computational costs for video applications. To mitigate these limitations while preserving the rich generative priors, existing DM-based VSR approaches typically leverage off-the-shelf diffusion models. For instance, DiffIR2VR [27] proposes a zero-shot framework that restores videos using pre-trained image restoration diffusion models, while subsequent works [13, 28, 14, 12] extend text-toimage diffusion models by incorporating temporal modules and fine-tuning the added parameters. Despite these efforts, alignment inaccuracies and suboptimal feature guidance still limit their performance, as detailed in Supplementary 1.

2.2 Alignment in VSR

A key distinction between VSR and SISR lies in VSR's capacity to exploit temporal information across multiple frames. However, early methods [29, 30, 31] often overlook the critical role of spatial alignment, which is essential for effective aggregation of highly correlated but misaligned frames or features.

Subsequent works have attempted to address this issue through various alignment strategies [15, 8, 5]. For instance, TOFlow [15] proposes a task-oriented flow network to warp input frames to their adjacent frames. EDVR [8] introduces deformable convolution to align features at multiple scales, while BasicVSR [5] employs optical flow to assist feature alignment. Inspired by prior works, subsequent works [9, 6] focus on flow-based alignment. PSRT [19] shows that Vision Transformers can directly process unaligned multi-frame inputs given sufficiently large window sizes and proposes a patch alignment method to optimize the performance-computation trade-off. Recently, IART [32] demonstrates that inaccurate warping degrades VSR performance and addresses this by designing a coordinate network to learn the warping function. However, in the context of DMbased VSR, the effectiveness of alignment strategies remains understudied. To tackle this challenge, this paper proposes a simple yet effective alignment strategy based on two insightful observations within the DM-based VSR pipeline.

3 Preliminaries and Observations

3.1 Diffusion Models for VSR

Diffusion models [33] use a Markov chain to convert variables from simple distributions (e.g., Gaussian) to complex distributions. In latent diffusion models (LDMs) [34], this process occurs in a low-resolution latent space created by an encoder $E(\cdot)$, and high-resolution frames are reconstructed by a decoder $\mathcal{D}(\cdot)$. Given latent features $z_0 \sim p_{data}$, the forward diffusion process gradually adds noise to these features, obtaining the noisy features z_t at diffusion step t directly from z_0 following:

$$z_t = \sqrt{\hat{\alpha}_t} z_0 + \sqrt{(1 - \hat{\alpha}_t)} \epsilon, \tag{1}$$

where $t \in [1, T]$, ϵ is the added Gaussian noise, and $\hat{\alpha}_t = \prod_{\tau=0}^t \alpha_{\tau}$, α_{τ} is the noise schedule. In the reverse process, taking z_T sampled from $\mathcal{N}(0, 1)$ as input, the noise component $\epsilon_{\theta}(z_t, t)$ at each diffusion step t is gradually estimated and removed through an iterative Markovian process. We can sample z_{t-1} as:

$$z_{t-1} = \frac{1}{\sqrt{\alpha_t}} (z_t - \frac{1 - \alpha_t}{\sqrt{1 - \hat{\alpha}_t}} \epsilon_{\theta}(z_t, t)) + \sigma_t \varepsilon.$$
 (2)

Here, $\varepsilon \sim \mathcal{N}(0, 1)$ and σ_t represents the variance schedule. In practice, according to Eq. 1, the noise-free approximation $\tilde{z}_{t\to 0}$ can be directly predicted by projecting the denoised features z_t to the initial state following:

$$\tilde{z}_{t\to 0} = \frac{1}{\sqrt{\hat{\alpha}_t}} (z_t - \sqrt{1 - \hat{\alpha}_t} \epsilon_{\theta}(z_t, t)). \tag{3}$$

The VSR problem can be articulated as follows: Given a sequence of N low-resolution frames $\{x^i\}_{i=1}^N \in \mathbb{R}^{N \times h \times w \times 3}$, the objective is to reconstruct a corresponding high-resolution sequence $\{y^i\}_{i=1}^N \in \mathbb{R}^{N \times sh \times sw \times 3}$, where s represents the rescaling factor.

3.2 Observations within DM-based Pipeline

Observation 1: The latent feature domain outshines the pixel domain in terms of spatial and temporal correlations. To verify this observation, we conduct experiments on

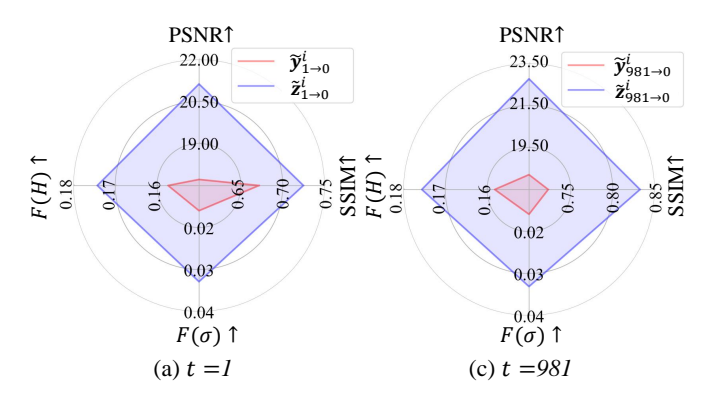


Figure 1: Illustration of average SSIM, PSNR, F(H) and $F(\sigma)$ metrics for adjacent variables across all frames in the REDS4 dataset, shown for diffusion steps (a) t = 1 and (b) t = 981.

the REDS4 dataset [35]. For the i-th frame at the t-th step, we employ a pre-trained DM-based VSR framework to extract two types of variables: the noise-free approximation feature $\tilde{z}_{t\to 0}^i$ predicted from z_t^i and the reconstructed high-resolution frame \tilde{y}_t^{i-1} . We adopt four metrics to compute the correlation: the Structural Similarity Index Measure (SSIM) [36], the Peak Signal-to-Noise Ratio (PSNR) [37], and the Cross-Entropy (H) [38] for pixellevel and distributional inter-variable correlation, as well as the Standard Deviation σ [39] for intra-variable correlation. To enable consistent comparison across all metrics, we transform H and σ into $F(H) = \frac{1}{1+H}$ and $F(\sigma) = \frac{1}{1+\sigma}$. In these transformed metrics, higher values indicate stronger correlations.

Figure 1 shows the average correlation metrics across all frames and features from diffusion steps t=1,981-th diffusion steps ¹ Results across multiple video samples from REDS4 consistently show that the latent feature domain outperforms the pixel domain in all four metrics. For instance, at the 981-th diffusion step, the average PSNR between adjacent features is 25.06% higher than that between adjacent frames. At the 1-th diffusion step, the $F(\sigma)$ value for features is 2.1 times that for frames. Averaged over all diffusion steps, the feature domain achieves improvements of 13.53% in PSNR, 22.61% in SSIM, 10.81% in F(H) and 106.50% in $F(\sigma)$ compared to the pixel domain. These results confirm that the latent feature domain provides significantly stronger spatial and temporal correlations, making it more suitable for guidance in DM-based VSR.

Although BasicVSR [5] also advocates feature-level guidance, we presents the first quantitative validation of this principle in the context of DM-based VSR. This observation directly motivates our design of dense feature-level guidance in DGAF-VSR. For a detailed comparison with BasicVSR, see Supplementary 2.

Observation 2: Warping at higher resolution better preserves high-frequency information, but only up to an optimal rescaling factor within the DM-based pipeline. Given the fact that high-frequency information critically influences super-resolution quality [40, 41, 42], we quantitatively analyze the high-frequency loss during warping. Our Observation 2 within DM-based VSR pipeline can be summarized as follows:

- Feature resolution directly affects high-frequency density.
- The warping operation reduces high-frequency density within features, while high-resolution features suffer less high-frequency degradation during warping compared to low-resolution features.
- The rescaling-based warping strategy effectively preserves the high-frequency information during alignment in DM-based VSR.
- An optimal rescaling exists for maximizing the highfrequency preservation of the rescaling-based warping strategy.

To validate Observation 2, we analyze over 80,000 feature groups from REDS4 using two high-frequency metrics: edge strength (computed with Canny [43], Sobel [44], and Laplacian [45] operators), and high-pass strength (computed as spectrum energy [46] after a Fast Fourier Transform (FFT) [47] followed by a high-pass filter with a threshold of 30). Higher values of both metrics indicate greater high-frequency density.

For the first point, we apply an $s \times$ upscaling and an $\frac{1}{s} \times$ downscaling operations on the original low-resolution features $\{\tilde{z}_{t\to 0}^i\}_{i=1,t=1}^{N,T}$ using nearest neighbor interpolation [48] ². This process obtains two transformed feature sets: the upscaled features $\{\tilde{z}_{t\to 0}^{i,s \times Ne}\}_{i=1,t=1}^{N,T}$ and the downscaled features $\{\tilde{z}_{t\to 0}^{i,s \times Ne}\}_{i=1,t=1}^{N,T}$. The edge strength and high-pass strength are calculated for these three sets, respectively. The results are illustrated in Figure 2 (a). As demonstrated, both metrics are sensitive to feature resolution. Therefore, all subsequent high-frequency analyses are conducted at a fixed resolution to ensure fair comparison.

For the second point, we implement bilinear warping on both $\{\tilde{z}_{t\to 0}^i\}_{i=1,t=1}^{N,T}$ and $\{\tilde{z}_{t\to 0}^{i,s\times Ne}\}_{i=1,t=1}^{N,T}$. The resulting warped features are denoted as $\{\tilde{z}_{t\to 0}^{i,warp}\}_{i=1,t=1}^{N,T}$ and $\{\tilde{z}_{t\to 0}^{i,s\times warp}\}_{i=1,t=1}^{N,T}$, respectively. As illustrated in Figure 2 (b), warping the low-resolution features causes a 12.68% reduction in edge strength and a 5.34% reduction in high-pass strength. In contrast, warping the high-resolution features leads to only a 4.38% loss in edge strength and a 1.75% loss in high-pass strength. These results indicate that although warping inevitably reduces high-frequency density, its impact is approximately three times milder when applied to high-resolution features than to low-resolution ones. This observation motivates our investigation of the third point.

For the third point, we process the rescaling-based warping features $\{\tilde{z}_{t\to 0}^{i,s \times warp \times \frac{1}{s}}\}_{i=1,t=1}^{N,T}$ through $\frac{1}{s} \times$ nearest neighbor interpolation-based downscaling on $\{\tilde{z}_{t\to 0}^{i,s \times warp}\}_{i=1,t=1}^{N,T}$. Figure 2 (c) shows the edge strength and high-pass strength of these downscaled features. Compared to directly warping the original low-resolution features, this upscale-warp-downscale strategy improves high-pass strength by 4.43% and edge strength by 9.98%.

Note that the edge strength presented in Figure 2 is computed using the Canny operator, complete analyses using the Sobel and Laplacian operators are included in Supplementary 3. In addition, the high-pass strength and edge strength across dif-

¹We select these steps to represent the early and late stages of the diffusion process.

²Note that *s* is chosen according to the fourth point.

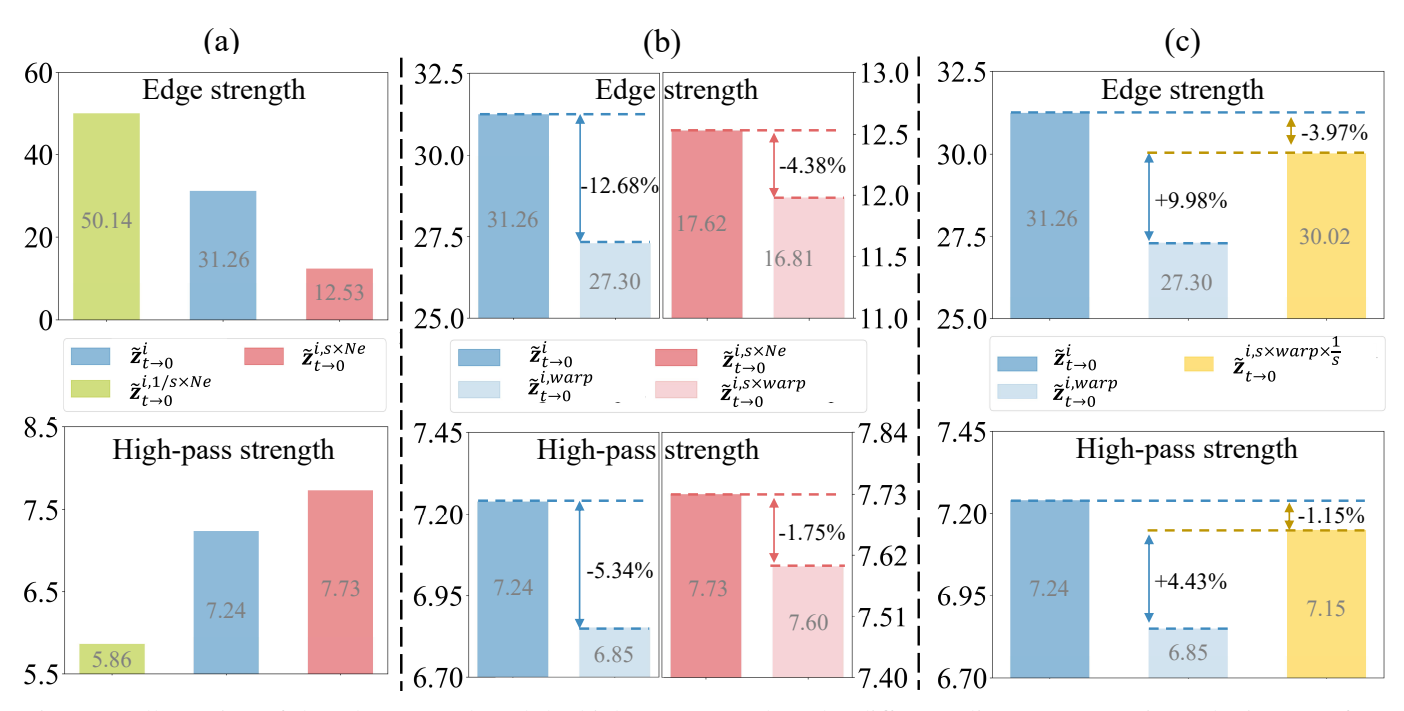


Figure 2: Illustration of the edge strength and the high-pass strength under different alignment strategies. The impact of (a) the upscaling and downscaling operations, (b) the warping operation on features of different resolutions, and (c) the upscaling—warping—downscaling strategy.

ferent diffusion steps are presented in Supplementary 4. Details regarding the fourth point are presented in Supplementary 5.

4 Метнор

Based on the observations established in Section 3.2, we present the Densely Guided diffusion model with Aligned Features for Video Super-Resolution (DGAF-VSR). The key ideas of our network are compared with those of MGLD-VSR [28] in Supplementary 6. As shown in Figure 3, DGAF-VSR consists of a Flow prediction Module (FM), T diffusion steps, and a pre-trained VAE decoder. The FM module utilizes a RAFT module [49] to calculate the compensatory optical flow $v^{i-1,i}$ between the upscaled adjacent frames $x^{i,s \times Ne}$ and $x^{i-1,s \times Ne}$. This process effectively captures motion patterns at a higher resolution. The sequence of diffusion steps can be partitioned into $\frac{T}{2}$ pairs. Each pair includes a forward guidance process (leveraging temporal information from previous features) and a backward guidance process (leveraging temporal information from subsequent features). Within each guidance process, the Optical Guided Warping Module (OGWM) is employed to align adjacent features, while the Feature-wise Temporal Condition Module (FTCM) is utilized to denoise current features under the dense guidance of aligned adjacent features. In the following, we describe the detailed architectures of these modules, using the forward guidance process as a representative example.

4.1 Optical Guided Warping Module

The Optical Guided Warping Module (OGWM) is built on **Observation 2**. While prior work (e.g., StableVSR [13]) demonstrates that direct motion compensation in latent space often introduces artifacts, our OGWM tackles the key challenges

of achieving accurate spatial alignment while preserving high-frequency information. As illustrated in Figure 3, the OGWM executes three stages during the forward guidance process in the *t*-th diffusion step: (a) **Input Preparation**: The OGWM module takes $\tilde{z}_{t\to 0}^{i-1}$ as input, which represents the noise-free approximation of the previous feature from the previous diffusion step. $\tilde{z}_{t\to 0}^{i-1}$ is upscaled by a factor of s=4 using nearest neighbor interpolation, resulting in $\tilde{z}_{t\to 0}^{i-1,s\times Ne}$. (b) **Feature Alignment**: The upscaled features $\tilde{z}_{t\to 0}^{i-1,s\times Ne}$ are warped using the computed optical flow $v^{i-1,i}$ to produce the aligned feature $\tilde{z}_{t\to 0}^{i-1,s\times warp}$ in the latent space. (c) **Downscaling and Integration**: The aligned features $\tilde{z}_{t\to 0}^{i-1,s\times warp}$ are downscaled by a factor of s to obtain $\tilde{z}_{t\to 0}^{i-1,s\times warp}$. Finally, $\tilde{z}_{t\to 0}^{i-1,s\times warp \times \frac{1}{s}}$ is fed into the FTCM module for dense feature guidance.

4.2 Feature-wise Temporal Condition Module

The Feature-wise Temporal Condition Module (FTCM) aggregates information from multiple frames and aligned features to provide dense motion compensation. Specifically, our guiding mechanism builds upon the analysis presented in **Observation 1** in Section 3.2 by utilizing adjacent features aligned through the OGWM module. Moreover, while existing DM-based superresolution methods typically employ only the U-Net encoder as the guiding network [13, 23, 28, 50], our FTCM incorporates the complete U-Net architecture. This design enables dense integration of adjacent information by introducing strict pixel-topixel constraints at different receptive fields during information extraction and reconstruction. By leveraging the full U-Net, we ensure more effective compensation of motion information, thereby allowing our proposed network to preserve fine-grained details and produce high-quality results.

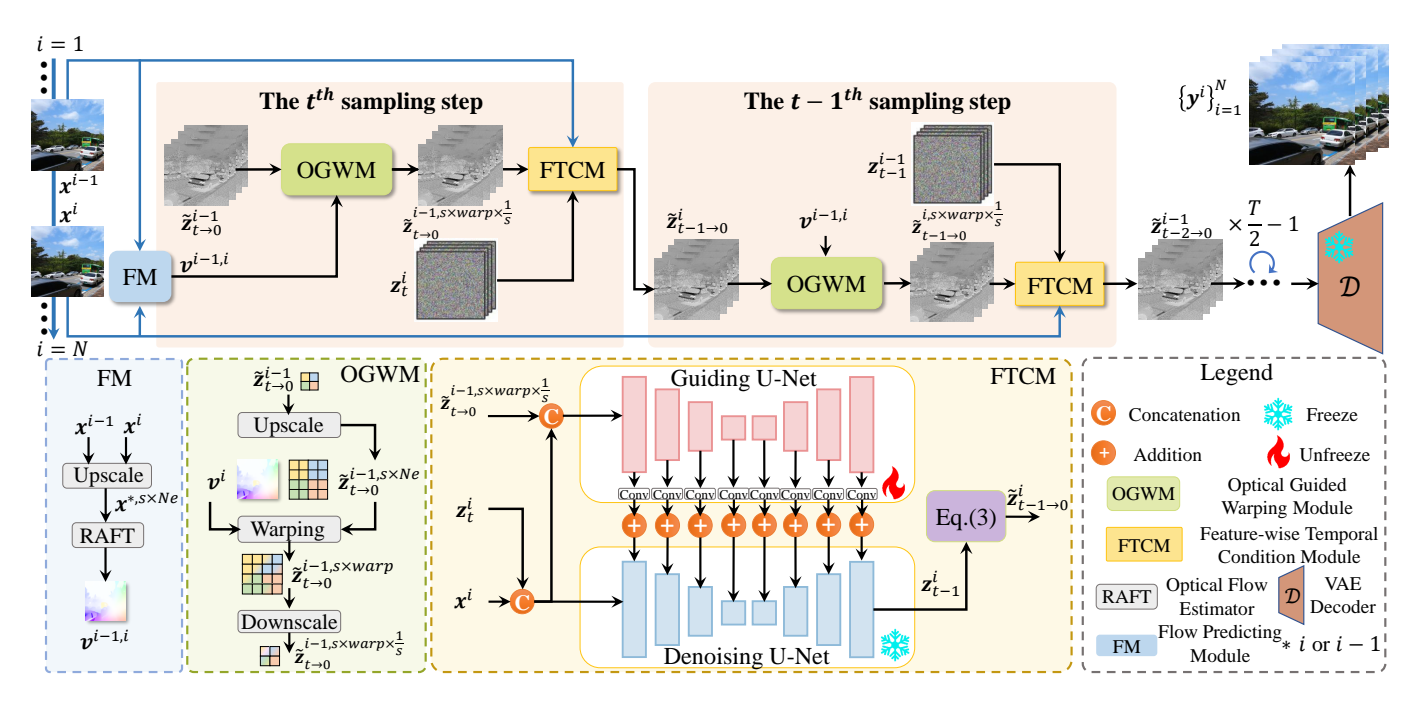


Figure 3: The framework of the proposed DGAF-VSR. The network is composed of a Flow prediction Module (FM), *T* diffusion steps, and a VAE decoder. The FM module estimates bidirectional optical flow estimation. Each diffusion step consists of one Optical Guided Warping Module (OGWM) module for feature warping process, and one Feature-wise Temporal Condition Module (FTCM) module for fine-grained information integration through dense feature guidance.

Within each diffusion step $t \in [1, T]$ of the DM model, the input low-resolution video is processed frame by frame. For instance, denoising of the *i*-th latent feature z_t^i at the *t*-th diffusion step is guided by the aligned adjacent feature $\tilde{z}_{t\to 0}^{i-1,s\times warp\times \frac{1}{s}}$ according to the following equation:

$$\boldsymbol{z}_{t-1}^{i} = DU(\left[\boldsymbol{z}_{t}^{i}, \boldsymbol{x}^{i}\right]) + Conv(GU(\left[\boldsymbol{z}_{t}^{i}, \boldsymbol{x}^{i}, \tilde{\boldsymbol{z}}_{t-0}^{i-1, s \times warp \times \frac{1}{s}}\right])). \tag{4}$$

 $DU(\cdot)$ denotes a pretrained Denoising U-Net with frozen parameters during training, while $GU(\cdot)$ represents the Guiding U-Net with parameters that are trainable throughout the training process, as shown in Figure 3. The notation $|z_t^i, x^i|$ signifies the concatenation of the current low-resolution frame x^i and the current latent feature z_t^i updated from the previous diffusion step t+1. Similarly, $\left[z_{t}^{i}, \mathbf{x}^{i}, z_{t\rightarrow0}^{i-1, s\times warp \times \frac{1}{s}}\right]$ indicates the concatenation of z_t^i, x^i and the aligned adjacent feature $\tilde{z}_{t\to 0}^{i-1,s\times warp \times \frac{1}{s}}$. The $Conv(\cdot)$ operation denotes a zero-initialized convolutional layer, which prevents the intermediate features in $DU(\cdot)$ from being overly influenced during the early training stages. Furthermore, in the *t*-th diffusion step, after we obtain the denoised features z_{t-1}^i , we can predict the noise-free approximation $\tilde{z}_{t-1\to 0}^i$ of the current feature through the reverse process described in Eq. (3). This noise-free approximation will be used as the guiding information for the adjacent frames in the next diffusion step. After T diffusion steps, the final denoised features $\{z_1^i\}_{i=1}^N$ are fed into a pretrained VAE decoder $\mathcal{D}(\cdot)$, yielding the high-resolution output frames $\{y^i\}_{i=1}^N$.

5 Experiments

5.1 Experimental Settings

The descriptions of the experimental settings for our DGAF-VSR are provided in Supplementary 7.

5.2 Comparison with State-of-the-art Methods

We evaluate the effectiveness of DGAF-VSR in comparison to eight state-of-the-art (SOTA) VSR methods, including four non-DM-based methods EDVR [8], BasicVSR [5], BasicVSR++ [9], and RVRT [6], as well as four DM-based methods StableVSR [13], MGLD-VSR [28], UAV [12] and STAR [51]. The quantitative and qualitative comparisons are carried out on the synthetic datasets REDS [35] and Vid4 [4], as well as the real-world dataset VideoLQ [10].

Quantitative Evaluation. The quantitative results on the synthetic datasets REDS4 and Vid4 are shown in Table 1. As can be seen, our DGAF-VSR achieves the best performance on all perceptual metrics, including both full-reference metrics (LPIPS, DISTS) and no-reference metrics (MUSIQ, CLIP-IQA, NIQE). Specifically, compared to the top-performing non-DM-based method, DGAF-VSR enhances the LPIPS metric by 25.78% on the REDS4 dataset. When compared to the SOTA DMbased method, DGAF-VSR achieves an improvement of 0.75 in MUSIQ on the Vid4 dataset. The impressive perceptual performance of DGAF-VSR reflects its strong capability to reconstruct realistic details and textures for the VSR task. In addition, compared to DM-based methods, our DGAF-VSR achieves the highest PSNR and SSIM scores on synthetic datasets, demonstrating a superior balance between fidelity and perceptual quality. Specifically, DGAF-VSR outperforms StableVSR by 0.20 dB in PSNR and 0.009 in SSIM for the REDS4 dataset, and by 0.28 dB

Table 1: Quantitative comparison on the REDS4 and Vid4 dataset for $4 \times VSR$ in terms of five perceptual(\diamond) and two fidelity metrics(\star), with the best results in bold and second bests underlined.

Dataset	Types	Methods	LPIPS◊↓	DISTS◊↓	MUSIQ⋄↑	CLIP-IQA◊↑	NIQE◊↓	PSNR★↑	SSIM⋆↑
		Bicubic	0.453	0.186	26.89	0.304	6.85	26.13	0.729
	Non-	EDVR [8]	0.178	0.082	65.44	0.367	4.15	31.02	0.879
	DM-	BasicVSR [5]	0.165	0.081	65.74	0.371	4.13	31.42	0.891
	based	BasicVSR++ [9]	0.132	0.069	67.00	0.381	3.85	32.39	0.907
	Daseu	RVRT [6]	0.128	0.067	67.46	0.392	3.78	32.75	0.911
REDS4		UAV [12]	0.266	0.124	47.94	0.193	4.69	26.09	0.724
		MGLD-VSR [28]	0.141	0.061	67.37	0.409	2.81	26.20	0.736
	DM- based	StableVSR [13]	0.098	0.045	<u>67.62</u>	0.418	<u>2.74</u>	27.97	0.795
		STAR [51]	0.285	0.117	66.54	0.266	3.45	23.01	0.644
		Ours	0.095	0.043	67.90	0.429	2.66	28.17	0.804
		Bicubic	0.497	0.242	26.54	0.342	7.55	23.78	0.635
	Non-	EDVR [8]	0.224	0.138	59.63	0.311	4.96	27.35	0.826
	DM-	BasicVSR [5]	0.214	0.136	60.90	0.320	4.88	27.24	0.825
	based	BasicVSR++ [9]	0.189	0.122	61.50	0.341	5.04	<u>27.79</u>	0.840
	baseu	RVRT [6]	0.188	0.114	61.84	0.374	4.89	27.99	0.846
Vid4		UAV [12]	0.340	0.204	63.21	0.264	3.78	22.14	0.537
		MGLD-VSR [28]	0.243	0.163	65.07	0.366	3.20	23.64	0.641
	DM-	StableVSR [13]	0.182	0.116	<u>67.20</u>	0.453	3.19	24.47	0.699
	based	STAR [51]	0.372	0.171	59.12	0.314	4.35	18.70	0.486
		Ours	0.175	0.113	67.95	0.470	3.10	24.75	0.714

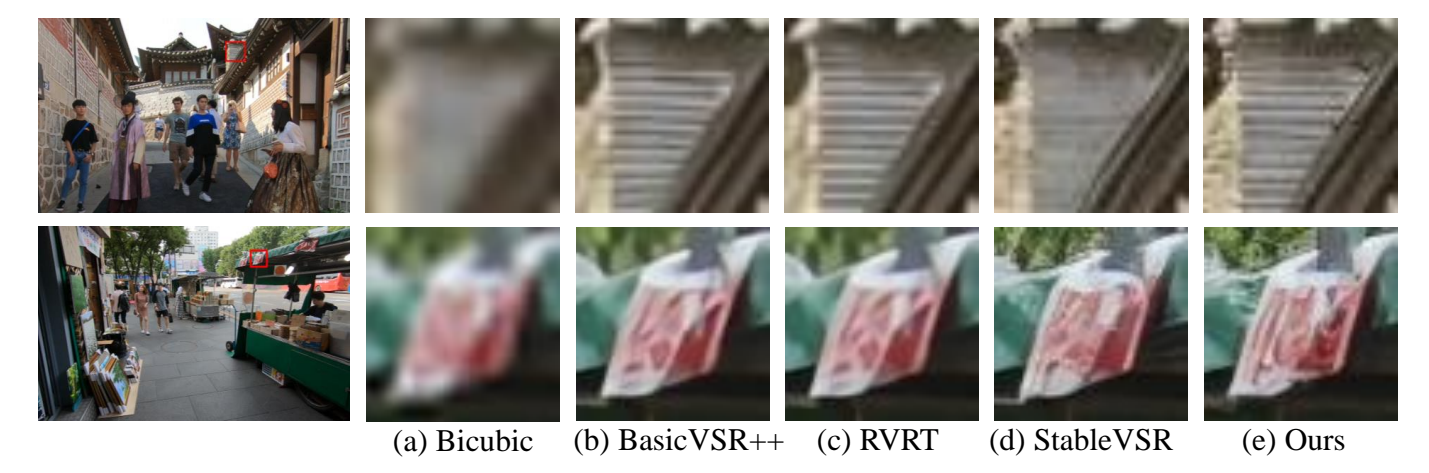


Figure 4: Visualization of the VSR results from different methods on REDS4 dataset.

in PSNR and 0.015 in SSIM for the Vid4 dataset. Furthermore, our DGAF-VSR demonstrates excellent VSR performance on the real-world VideoLQ dataset, as shown in Table 2. Specifically, DGAF-VSR outperforms STAR by 4.46 in MUSIQ value and 59.11% in CLIP-IQA value. These quantitative results confirm the superior reconstruction ability of our proposed network in VSR. Comparisons of VSR performance at different scale factors are presented in Supplementary 8.

Table 2: Quantitative comparison on the VideoLQ for 4× VSR in terms of three perceptual metrics, with the best results in bold.

Method	MUSIQ↑	CLIP-IQA↑	DOVER↑
UAV [12]	30.88	0.182	0.4493
MGLD-VSR [28]	55.99	0.339	0.7254
STAR [51]	54.59	0.313	0.7034
Ours	59.05	0.498	0.7599

Qualitative Evaluation. Figure 4 visualizes the 4× VSR results of different methods on the REDS4 dataset. As can be seen, our method effectively maintains high-frequency information while recovering realistic image details, such as the texture of the wall and the patterns on the food trolley signs. In contrast, other approaches suffer from blurred edges [9, 6] or unrealistic details [13]. Additional comparisons on the Vid4 dataset are provided in the Supplementary 9. Descriptions of the high-frequency preservation capabilities of DGAF-VSR are shown in Supplementary 10.

5.3 Temporal Consistency of DGAF-VSR

According to Observation 1, our approach leverages strong inter- and intra-variable correlations to achieve superior temporal consistency in VSR results. In this section, we systematically validate this advantage. As shown in Figure 5, we evaluate the temporal consistency metrics tLPIPS [52] and tOF [52] for the VSR output sequences on the REDS4 dataset across different approaches. Specifically, our approach shows a 56.30% improvement in tLPIPS over RVRT, a SOTA non-DM-based method. In addition, compared to the SOTA DM-based method Stable VSR, our approach improves tLPIPS by 30.37% and tOF by 2.02%. Furthermore, in Figure 6, we show a comparison of the temporal profiles between our DGAF-VSR and SOTA DM-based methods UAV, MGLD and StableVSR. As illustrated, the profiles from UAV and MGLD exhibit noticeable noise, indicating flickering artifacts. The profile from StableVSR still shows visible discontinuities, while the profile of our approach exhibits a more seamless and smoother transition. These quantitative gains and qualitative observations collectively confirm the effectiveness of our feature alignment and dense guidance mechanism in enhancing temporal consistency.

5.4 Efficiency of DGAF-VSR

The running efficiency of the network is a crucial factor to consider for practical applications. We present the runtime, network parameters, and the GPU memory overhead of DGAF-VSR in Supplementary 11.

5.5 Ablation Study

In this subsection, we analyze the effects of several crucial components on the proposed DGAF-VSR, including the

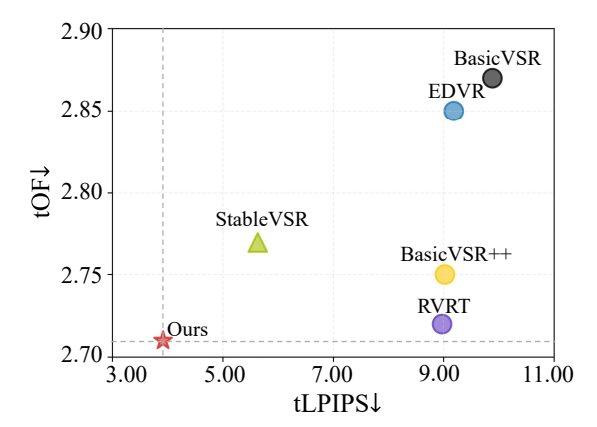


Figure 5: The temporal consistency results for VSR on REDS4 dataset.

rescaling-based warping strategy in the OGWM modules, the dense guidance mechanism in the FTCM modules, the in-pair forward and backward guidance strategy, the pre-upscaling strategy, the choice of optical flow estimator and the rescaling factor. All ablation studies are conducted on the REDS dataset, and the analyzes of the last four ablation studies are provided in the Supplementary 12.

Effect of the dense guidance mechanism. As shown in Table 3, a comparison between case 1 and case 4 evaluates the 4× VSR performance with and without the dense guidance mechanism. Incorporating this strategy improves PSNR by 0.36 dB, lowers the LPIPS score by 0.009, and reduces tLPIPS score by 37.28%, indicating significant improvements in fidelity, perceptual quality, and temporal consistency. In conclusion, these results substantiate the effectiveness of the dense guidance mechanism.

Effect of the rescaling-based warping strategy. The case 2, case 3 and case 4 in Table 3 compare the effects of bicubic and nearest neighbor interpolation operations. Specifically, in case 2, when the warping process is applied to the original features without any interpolation, the PSNR value is 26.70 dB, with an SSIM of 0.756, an LPIPS of 0.118, and a tOF of 3.29. In case 3, employing the bicubic interpolation method improves the VSR performance, yielding a PSNR of 28.13 dB, an SSIM of 0.803, and decreases the LPIPS and tOF to 0.099 and 2.81, respectively. Furthermore, our proposed method using nearest neighbor interpolation, as shown in case 4, achieves the highest PSNR of 28.17 dB, an SSIM value of 0.804, and the lowest LPIPS and tOF, which are 0.095 and 2.71 respectively. These results suggest that performing warping at a higher resolution significantly enhances VSR performance, while nearest neighbor interpolation outperforms bicubic interpolation by better preserving spatial details and temporal coherence.

6 Conclusion

In this paper, we propose DGAF-VSR, a novel diffusion model (DM)-based network for video super-resolution (VSR). Our method significantly enhances perceptual quality and reconstruction fidelity while maintaining robust temporal consistency. Within the DM-based pipeline, we identify two key observations: (a) the feature domain exhibits stronger spatial and tem-

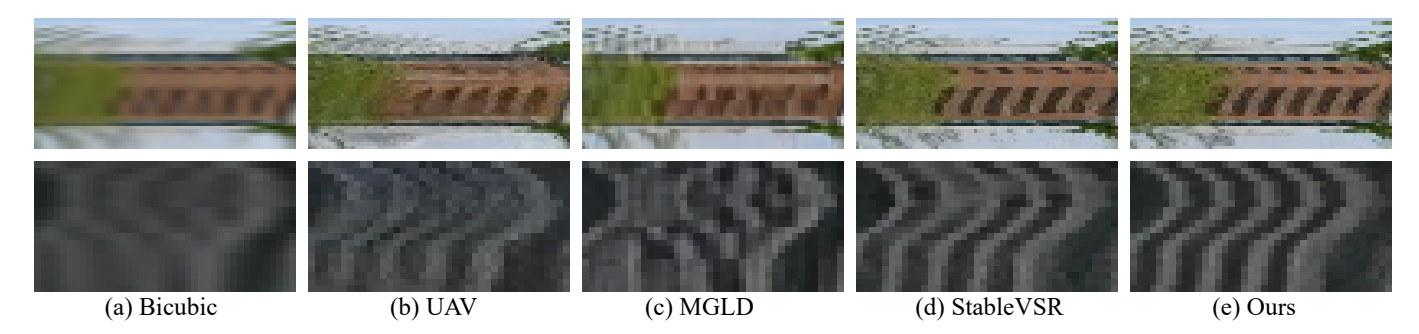


Figure 6: Visualization of the temporal profiles from different methods on REDS4 dataset. We examine a row and track changes across adjacent frames over time.

Table 3: The effect of the dense guidance mechanism and the rescaling-based warping strategy, in terms of two perceptual (\diamond) , two fidelity (\star) and two temporal consistency (\diamond) metrics, with the best results in bold and second bests underlined.

Case	Bicubic	Nearest	Dense guidance	PSNR ⋆ ↑	SSIM ⋆ ↑	LPIPS◊ ↓	DISTS♦↓	tLPIPS∘↓	tOF∘↓
1		√		27.81	0.791	0.104	0.047	6.25	2.83
2			✓	26.70	0.756	0.118	0.050	21.61	3.29
3	✓		✓	28.13	0.803	0.099	0.045	4.28	2.81
4(Ours)		\checkmark	✓	28.17	$\overline{0.804}$	0.095	$\overline{0.043}$	3.92	2.71

poral correlations than the pixel domain, and (b) warping at an upscaled resolution is highly effective for preserving high-frequency information during alignment, but this improvement is not necessarily monotonic. Leveraging these two observations, for each diffusion step within the DM-based pipeline, we develop an optical guided warping module (OGWM) for precise feature alignments, as well as a feature-wise temporal condition module (FTCM) for dense guidance from adjacent features. Experimental results demonstrated that our DGAF-VSR achieved state-of-the-art VSR performance in terms of perceptual quality, fidelity, and temporal consistency. Exploring more effective feature warping and dense guidance mechanisms across a broader range of video restoration tasks presents a promising direction for future research.

REFERENCES

- [1] Simon Baker and Takeo Kanade. Super-resolution optical flow, volume 510. Carnegie Mellon University, The Robotics Institute Pittsburgh, 1999.
- [2] Rik Fransens, Christoph Strecha, and Luc Van Gool. Optical flow based super-resolution: A probabilistic approach.

 Computer vision and image understanding, 106(1):106–115, 2007.
- [3] Thomas Brox, Andrés Bruhn, Nils Papenberg, and Joachim Weickert. High accuracy optical flow estimation based on a theory for warping. In Computer Vision-ECCV 2004: 8th European Conference on Computer Vision, Prague, Czech Republic, May 11-14, 2004. Proceedings, Part IV 8, pages 25–36. Springer, 2004.
- [4] Ce Liu and Deqing Sun. On bayesian adaptive video super resolution. IEEE transactions on pattern analysis and machine intelligence, 36(2):346–360, 2013.
- [5] Kelvin CK Chan, Xintao Wang, Ke Yu, Chao Dong, and Chen Change Loy. BasicVSR: The search for essential

- components in video super-resolution and beyond. In Proceedings of the IEEE/CVF conference on computer vision and pattern recognition, pages 4947–4956, 2021.
- [6] Jingyun Liang, Yuchen Fan, Xiaoyu Xiang, Rakesh Ranjan, Eddy Ilg, Simon Green, Jiezhang Cao, Kai Zhang, Radu Timofte, and Luc V Gool. Recurrent video restoration transformer with guided deformable attention. <u>Advances</u> in Neural Information Processing Systems, 35:378–393, 2022.
- [7] Yapeng Tian, Yulun Zhang, Yun Fu, and Chenliang Xu. TDAN: Temporally-deformable alignment network for video super-resolution. In Proceedings of the IEEE/CVF conference on computer vision and pattern recognition, pages 3360–3369, 2020.
- [8] Xintao Wang, Kelvin CK Chan, Ke Yu, Chao Dong, and Chen Change Loy. EDVR: Video restoration with enhanced deformable convolutional networks. In Proceedings of the IEEE/CVF conference on computer vision and pattern recognition workshops, pages 0–0, 2019.
- [9] Kelvin CK Chan, Shangchen Zhou, Xiangyu Xu, and Chen Change Loy. Basicvsr++: Improving video superresolution with enhanced propagation and alignment. In <u>Proceedings of the IEEE/CVF conference on computer</u> vision and pattern recognition, pages 5972–5981, 2022.
- [10] Kelvin CK Chan, Shangchen Zhou, Xiangyu Xu, and Chen Change Loy. Investigating tradeoffs in real-world video super-resolution. In Proceedings of the IEEE/CVF Conference on Computer Vision and Pattern Recognition, pages 5962–5971, 2022.
- [11] Xingyu Zhou, Leheng Zhang, Xiaorui Zhao, Keze Wang, Leida Li, and Shuhang Gu. Video super-resolution transformer with masked inter&intra-frame attention. In Proceedings of the IEEE/CVF Conference on Computer

- 2024.
- [12] Shangchen Zhou, Peiqing Yang, Jianyi Wang, Yihang Luo, and Chen Change Loy. Upscale-A-Video: Temporalconsistent diffusion model for real-world video superresolution. In Proceedings of the IEEE/CVF Conference on Computer Vision and Pattern Recognition, pages 2535– 2545, 2024.
- [13] Claudio Rota, Marco Buzzelli, and Joost van de Weijer. Enhancing perceptual quality in video super-resolution through temporally-consistent detail synthesis using diffusion models. In European Conference on Computer Vision, pages 36–53. Springer, 2024.
- [14] Zhikai Chen, Fuchen Long, Zhaofan Qiu, Ting Yao, Wengang Zhou, Jiebo Luo, and Tao Mei. Learning spatial adaptation and temporal coherence in diffusion models for video super-resolution. In Proceedings of the IEEE/CVF Conference on Computer Vision and Pattern Recognition, pages 9232–9241, 2024.
- [15] Tianfan Xue, Baian Chen, Jiajun Wu, Donglai Wei, and William T Freeman. Video enhancement with task-oriented flow. International Journal of Computer Vision, 127:1106-1125, 2019.
- [16] Jifeng Dai, Haozhi Qi, Yuwen Xiong, Yi Li, Guodong Zhang, Han Hu, and Yichen Wei. Deformable convolutional networks. In Proceedings of the IEEE international conference on computer vision, pages 764–773, 2017.
- [17] Jiezhang Cao, Yawei Li, Kai Zhang, and Luc Van Gool. Video super-resolution transformer. arXiv preprint arXiv:2106.06847, 2021.
- [18] Jingyun Liang, Jiezhang Cao, Yuchen Fan, Kai Zhang, Rakesh Ranjan, Yawei Li, Radu Timofte, and Luc Van Gool. VRT: A video restoration transformer. IEEE Transactions on Image Processing, 2024.
- [19] Shuwei Shi, Jinjin Gu, Liangbin Xie, Xintao Wang, Yujiu Yang, and Chao Dong. Rethinking alignment in video super-resolution transformers. Advances in Neural Information Processing Systems, 35:36081–36093, 2022.
- [20] Yiran Xu, Taesung Park, Richard Zhang, Yang Zhou, Eli Shechtman, Feng Liu, Jia-Bin Huang, and Difan Liu. Videogigagan: Towards detail-rich video super-resolution. arXiv preprint arXiv:2404.12388, 2024.
- [21] Minguk Kang, Jun-Yan Zhu, Richard Zhang, Jaesik Park, Eli Shechtman, Sylvain Paris, and Taesung Park. Scaling up gans for text-to-image synthesis. In Proceedings of the IEEE/CVF conference on computer vision and pattern recognition, pages 10124-10134, 2023.
- [22] Chitwan Saharia, Jonathan Ho, William Chan, Tim Salimans, David J Fleet, and Mohammad Norouzi. Image super-resolution via iterative refinement. transactions on pattern analysis and machine intelligence, 45(4):4713–4726, 2022.
- [23] Jianyi Wang, Zongsheng Yue, Shangchen Zhou, Kelvin CK Chan, and Chen Change Loy. Exploiting diffusion prior for real-world image super-resolution. International Journal of Computer Vision, 132(12):5929-5949, 2024.

- Vision and Pattern Recognition, pages 25399–25408, [24] Zongsheng Yue, Kang Liao, and Chen Change Loy. Arbitrary-steps image super-resolution via diffusion inversion. arXiv preprint arXiv:2412.09013, 2024.
 - [25] Zongsheng Yue, Jianyi Wang, and Chen Change Loy. ResShift: Efficient diffusion model for image superresolution by residual shifting. Advances in Neural Information Processing Systems, 36:13294–13307, 2023.
 - Rongyuan Wu, Lingchen Sun, Zhiyuan Ma, and Lei Zhang. One-step effective diffusion network for real-world image super-resolution. Advances in Neural Information Processing Systems, 37:92529-92553, 2024.
 - Chang-Han Yeh, Chin-Yang Lin, Zhixiang Wang, Chi-Wei Hsiao, Ting-Hsuan Chen, Hau-Shiang Shiu, and Yu-Lun Liu. Diffir2vr-zero: Zero-shot video restoration with diffusion-based image restoration models. arXiv preprint arXiv:2407.01519, 2024.
 - [28] Xi Yang, Chenhang He, Jianqi Ma, and Lei Zhang. Motionguided latent diffusion for temporally consistent realworld video super-resolution. In European Conference on Computer Vision, pages 224–242. Springer, 2024.
 - [29] Yan Huang, Wei Wang, and Liang Wang. Video superresolution via bidirectional recurrent convolutional networks. IEEE transactions on pattern analysis and machine intelligence, 40(4):1015–1028, 2017.
 - [30] Dario Fuoli, Shuhang Gu, and Radu Timofte. Efficient video super-resolution through recurrent latent space propagation. In 2019 IEEE/CVF International Conference on Computer Vision Workshop (ICCVW), pages 3476–3485. IEEE, 2019.
 - [31] Younghyun Jo, Seoung Wug Oh, Jaeyeon Kang, and Seon Joo Kim. Deep video super-resolution network using dynamic upsampling filters without explicit motion compensation. In Proceedings of the IEEE conference on computer vision and pattern recognition, pages 3224– 3232, 2018.
 - [32] Kai Xu, Ziwei Yu, Xin Wang, Michael Bi Mi, and Angela Yao. Enhancing video super-resolution via implicit resampling-based alignment. In Proceedings of the IEEE/CVF Conference on Computer Vision and Pattern Recognition, pages 2546–2555, 2024.
 - [33] Jonathan Ho, Ajay Jain, and Pieter Abbeel. Denoising diffusion probabilistic models. arXiv preprint arxiv:2006.11239, 2020.
 - [34] Robin Rombach, Andreas Blattmann, Dominik Lorenz, Patrick Esser, and Björn Ommer. High-resolution image synthesis with latent diffusion models. In Proceedings of the IEEE/CVF conference on computer vision and pattern recognition, pages 10684-10695, 2022.
 - [35] Seungjun Nah, Sungyong Baik, Seokil Hong, Gyeongsik Moon, Sanghyun Son, Radu Timofte, and Kyoung Mu Lee. Ntire 2019 challenge on video deblurring and superresolution: Dataset and study. In Proceedings of the IEEE/CVF conference on computer vision and pattern recognition workshops, pages 0–0, 2019.
 - [36] Zhou Wang, Alan C Bovik, Hamid R Sheikh, and Eero P Simoncelli. Image quality assessment: from error visibility to structural similarity. IEEE transactions on image processing, 13(4):600-612, 2004.

- [37] Alain Hore and Djemel Ziou. Image quality metrics: [53] Robin Rombach, Andreas Blattmann, Dominik Lorenz, PSNR vs. SSIM. In 2010 20th international conference on pattern recognition, pages 2366–2369. IEEE, 2010.
- [38] Claude E Shannon. A mathematical theory of communication. The Bell system technical journal, 27(3):379-423,
- [39] Douglas G Altman and J Martin Bland. Standard deviations and standard errors. Bmj, 331(7521):903, 2005.
- [40] Fuqiang Zhou, Xiaojie Li, and Zuoxin Li. frequency details enhancing densenet for super-resolution. Neurocomputing, 290:34-42, 2018.
- [41] Ao Li, Le Zhang, Yun Liu, and Ce Zhu. Feature modulation transformer: Cross-refinement of global representation via high-frequency prior for image super-resolution. In Proceedings of the IEEE/CVF International Conference on Computer Vision, pages 12514–12524, 2023.
- [42] Manuel Fritsche, Shuhang Gu, and Radu Timofte. Frequency separation for real-world super-resolution. In 2019 IEEE/CVF International Conference on Computer Vision Workshop (ICCVW), pages 3599–3608. IEEE, 2019.
- [43] John Canny. A computational approach to edge detection. IEEE Transactions on pattern analysis and machine intelligence, (6):679-698, 1986.
- [44] Irwin Sobel, Gary Feldman, et al. A 3x3 isotropic gradient operator for image processing. a talk at the Stanford Artificial Project in, 1968:271-272, 1968.
- [45] Ramesh Jain, Rangachar Kasturi, Brian G Schunck, et al. Machine vision, volume 5. McGraw-hill New York, 1995.
- [46] van A Van der Schaaf and JH van van Hateren. Modelling the power spectra of natural images: statistics and information. Vision research, 36(17):2759–2770, 1996.
- [47] Henri J Nussbaumer and Henri J Nussbaumer. The fast Fourier transform. Springer, 1982.
- [48] Donald Shepard. A two-dimensional interpolation function for irregularly-spaced data. In Proceedings of the 1968 23rd ACM national conference, pages 517–524, 1968.
- [49] Zachary Teed and Jia Deng. RAFT: Recurrent allpairs field transforms for optical flow. In Computer Vision–ECCV 2020: 16th European Conference, Glasgow, UK, August 23-28, 2020, Proceedings, Part II 16, pages 402–419. Springer, 2020.
- [50] Jingwen He, Tianfan Xue, Dongyang Liu, Xinqi Lin, Peng Gao, Dahua Lin, Yu Qiao, Wanli Ouyang, and Ziwei Liu. VEnhancer: Generative space-time enhancement for video generation. arXiv preprint arXiv:2407.07667, 2024.
- [51] Rui Xie, Yinhong Liu, Penghao Zhou, Chen Zhao, Jun Zhou, Kai Zhang, Zhenyu Zhang, Jian Yang, Zhenheng Yang, and Ying Tai. Star: Spatial-temporal augmentation with text-to-video models for real-world video superresolution. arXiv preprint arXiv:2501.02976, 2025.
- [52] Mengyu Chu, You Xie, Jonas Mayer, Laura Leal-Taixé, and Nils Thuerey. Learning temporal coherence via self-supervision for gan-based video generation. ACM Transactions on Graphics (TOG), 39(4):75–1, 2020.

- Patrick Esser, and Björn Ommer. High-resolution image synthesis with latent diffusion models. In Proceedings of the IEEE/CVF conference on computer vision and pattern recognition, pages 10684-10695, 2022.
- [54] Stability stabilityai/stable-diffusion-x4upscaler. https://huggingface.co/stabilityai/ stable-diffusion-x4-upscaler, 2022.
- [55] Andreas Blattmann, Tim Dockhorn, Sumith Kulal, Daniel Mendelevitch, Maciej Kilian, Dominik Lorenz, Yam Levi, Zion English, Vikram Voleti, Adam Letts, et al. Stable video diffusion: Scaling latent video diffusion models to large datasets. arXiv preprint arXiv:2311.15127, 2023.
- [56] Lymin Zhang, Anyi Rao, and Maneesh Agrawala. Adding conditional control to text-to-image diffusion models. In Proceedings of the IEEE/CVF international conference on computer vision, pages 3836-3847, 2023.
- [57] Richard Zhang, Phillip Isola, Alexei A Efros, Eli Shechtman, and Oliver Wang. The unreasonable effectiveness of deep features as a perceptual metric. In Proceedings of the IEEE conference on computer vision and pattern recognition, pages 586–595, 2018.
- [58] Keyan Ding, Kede Ma, Shiqi Wang, and Eero P Simoncelli. Image quality assessment: Unifying structure and texture similarity. IEEE transactions on pattern analysis and machine intelligence, 44(5):2567-2581, 2020.
- [59] Junjie Ke, Qifei Wang, Yilin Wang, Peyman Milanfar, and Feng Yang. MUSIQ: Multi-scale image quality transformer. In Proceedings of the IEEE/CVF international conference on computer vision, pages 5148–5157, 2021.
- [60] Jianyi Wang, Kelvin CK Chan, and Chen Change Loy. Exploring clip for assessing the look and feel of images. In Proceedings of the AAAI conference on artificial intelligence, volume 37, pages 2555–2563, 2023.
- [61] Anish Mittal, Rajiv Soundararajan, and Alan C Bovik. Making a "completely blind" image quality analyzer. IEEE Signal processing letters, 20(3):209–212, 2012.
- [62] Xiaohui Li, Yihao Liu, Shuo Cao, Ziyan Chen, Shaobin Zhuang, Xiangyu Chen, Yinan He, Yi Wang, and Yu Qiao. Diffvsr: Enhancing real-world video super-resolution with diffusion models for advanced visual quality and temporal consistency. arXiv e-prints, pages arXiv-2501, 2025.
- [63] Dustin Podell, Zion English, Kyle Lacey, Andreas Blattmann, Tim Dockhorn, Jonas Müller, Joe Penna, and Robin Rombach. SDXL: Improving latent diffusion models for high-resolution image synthesis. arXiv preprint arXiv:2307.01952, 2023.
- [64] Patrick Esser, Sumith Kulal, Andreas Blattmann, Rahim Entezari, Jonas Müller, Harry Saini, Yam Levi, Dominik Lorenz, Axel Sauer, Frederic Boesel, et al. Scaling rectified flow transformers for high-resolution image synthesis. In Forty-first international conference on machine learning, 2024.

SUPPLEMENTARY MATERIAL

1 Limitations of Existing Diffusion Model-based VSR

Instead of training from scratch, existing diffusion model (DM)-based VSR methods typically employ pre-trained textto-image diffusion models [53, 54, 55] as priors. However, the direct application of image-oriented methods introduces flickering artifacts to the VSR results, and the inherent randomness of the diffusion process aggravates this issue. Recent approaches including UAV [12], MGLD-VSR [28] and SATeCo [14] address temporal consistency by processing multiple frames using 3D CNNs or temporal attentions. Although these methods improve temporal stability, they require substantial computational resources, e.g., UAV [12] utilizes 32 NVIDIA A100-80G GPUs and 37K HD videos for training. Following the framework represented by BasicVSR[5], StableVSR [13] makes new attempts to incorporate bidirectional propagation with ControlNet-based [56] guidance during each diffusion step. Although the bidirectional guiding mechanism helps improve temporal consistency and mitigates error accumulation during diffusion process, StableVSR still suffers from the following limitations: (a) Inaccurate alignment in the pixel domain generates spatial artifacts that degrade fidelity, and the frame reconstruction process introduces unnecessary computational redundancy. (b) Limited guidance from U-Net encoder fails to provide sufficient inter-frame information compensation in pixel-to-pixel VSR task, leading to a perceptual-fidelity trade-off dilemma.

2 Comparison of Observation 1 and BasicVSR

The differences between our Observation 1 and BasicVSR are evident in the application architecture, empirical analysis, and conclusions regarding contributory factors, as shown in Table 1.

- (1) **Application Architecture.** BasicVSR investigates feature alignment in a non-generative pipeline (non-diffusion-based), where features are directly extracted from a convolutional neural network. In contrast, our work explores in a diffusion-based pipeline, where features are progressively generated and embedded into stochastic noise during the diffusion process. To our knowledge, bservation 1 constitutes the first comprehensive exploration of the interplay between feature and pixel domains within the context of diffusion-based video superresolution (VSR) pipeline.
- (2) **Empirical Analysis.** Basic VSR derives its analysis of feature and image alignment solely from VSR performance, noting a PSNR drop of 0.17 dB due to image alignment. In contrast, our analysis begins at the representation level: we systematically compare intra- and inter-frame correlations between feature and pixel domains across four quantitative metrics, offering direct evidence of their structural differences.
- (3) **Conclusions of Contributory Factor.** BasicVSR claims that the reason for the poorer performance of image alignment 'resulting from the inaccuracy of optical flow estimation'. However, since both feature and pixel warping rely on the same optical flow (computed from the input frames), any flow errors would degrade both warped features and warped frames

similarly. Therefore, the inaccuracy of optical flow estimation cannot explain why feature-domain alignment consistently outperforms pixel-domain alignment. In contrast, our work provides numerical evidence that the intra- and inter-frame correlations are significantly stronger in the feature domain. This stronger correlation could be a fundamental reason for the superior performance of feature alignment in diffusion-based video super-resolution (VSR).

3 Edge Strength Based on Different Operators

Figure 1 compares edge strength across different alignment processes using three standard edge detectors: Canny, Sobel, and Laplacian. As demonstrated, despite variations in absolute numerical values across operators, all three operators produce consistent rankings in quantifying edge strength. This pattern strongly supports the first three key points presented in bservation 2 of Section 3.2 of the manuscript.

Focusing on the second key point in bservation 2, Figure 1 (b) presents a comprehensive comparison of edge strength degradation across two distinct scenarios: (1) low-resolution features $\{\tilde{z}_{t\to 0}^i\}_{i=1,t=1}^{N,T}$ and warped low-resolution features $\{\tilde{z}_{t\to 0}^{i,sxNe}\}_{i=1,t=1}^{N,T}$ and warped high-resolution features $\{\tilde{z}_{1\to 0}^{i,sxNe}\}_{i=1,t=1}^{N,T}$. Specifically, warping on low-resolution features induces substantial edge strength degradation under all edge detection operators by 12.68% for Canny, 9.23% for Sobel, and 65.08% for Laplacian. In contrast, high-resolution feature warping shows markedly better preservation of edge information, reducing the degradation to just 4.38%, 5.52% and 40.69% for Canny, Sobel and Laplacian operators, respectively.

Regarding the third key point in bservation 2, Figure 1 (c) compares edge strength measurements across three feature representations: original low-resolution features $\{\tilde{z}_{t\to 0}^i\}_{i=1,t=1}^{N,T}$, warped low-resolution features $\{\tilde{z}_{t\to 0}^{i,warp}\}_{i=1,t=1}^{N,T}$, and downscaled features $\{\tilde{z}_{t\to 0}^{i,s\times warp \times \frac{1}{s}}\}_{i=1,t=1}^{N,T}$ after warping on high-resolution features. The results demonstrate that performing the rescaling-based warping strategy significantly enhances edge preservation by 9.98%, 5.78% and 43.89% under Canny, Sobel and Laplacian based edge strength measurement, respectively.

4 High-pass Strength and Edge Strength across Different Diffusion Steps

Figure 2 illustrates the results of the high-pass strength and edge strength averaged on the features $\{\tilde{z}_{t\to 0}^i\}_{i=1}^N, \{\tilde{z}_{t\to 0}^{i,warp}\}_{i=1}^N, \text{ and } \{\tilde{z}_{t\to 0}^{i,s\times warp\times\frac{1}{s}}\}_{i=1}^N$ at different diffusion steps t. As shown, at all diffusion steps, the rescaling-based warping strategy (denoted as $s\times warp\times\frac{1}{s}$) preserves more high-frequency information compared to directly warping on the original resolution(warp). As the reverse process progresses (i.e., as t decreases), the high-frequency density measured by multiple indicators steadily increases. This implies that high-frequency information is gradually introduced into the low-resolution with the denoising and guiding process, which is in line with the principle of the diffusion model.

Table 1: Comparion of bservation 1 and BasicVSR.

Method	BasicVSR	Ours			
Application Architecture	CNN-based Network	Diffusion-based Network			
Empirical Analysis	VSR performance	Data Analysis & VSR performance			
Contributory Factors	Stronger optical flow estimation	Stronger intra- and inter-frame correlations			

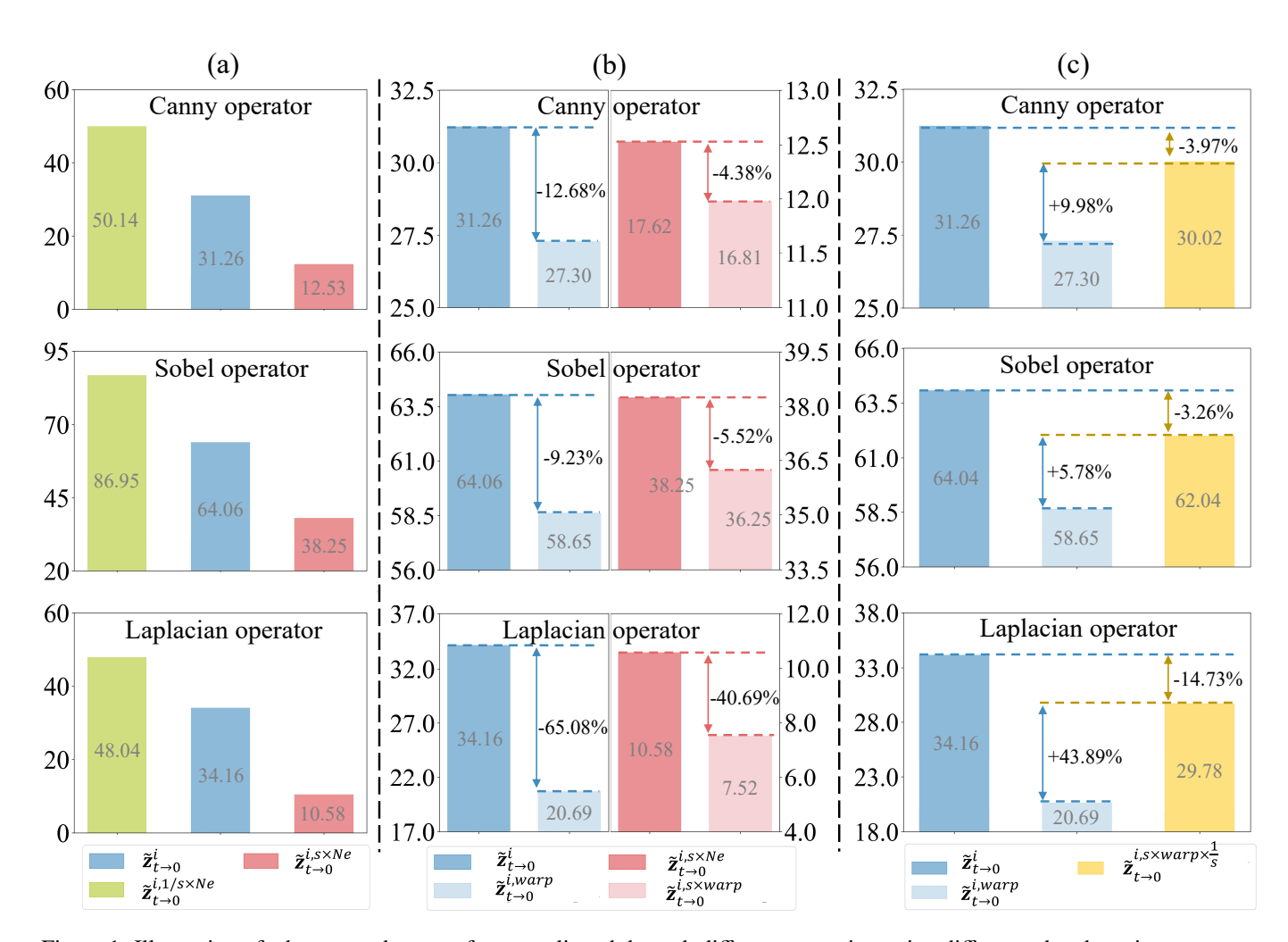


Figure 1: Illustration of edge strength across features aligned through different strategies, using different edge detection operators including the Canny, Sobel, and Laplacian, from top to bottom. (a) the upscaling and downscaling operations, (b) the warping operation on features of different resolutions, and (c) the rescaling-based warping strategy.

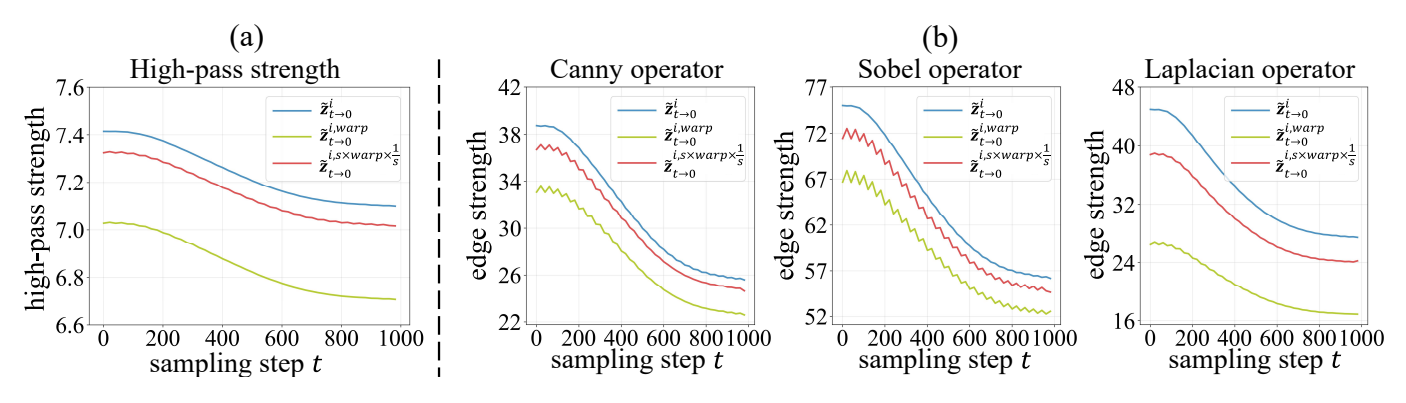


Figure 2: Illustration of high-pass strength and edge strength across different diffusion steps.

5 THE OPTIMAL RESCALING FACTOR OF THE RESCALING-BASED WARPING STRATEGY

Figure 3 shows the impact of the rescaling factor in the rescaling-based warping strategy on VSR tasks at different scales. As shown in the top row, the reduction ratio of edge strength during warping decreases as the rescaling factor increases, and this reduction gradually saturates. Moreover, the bottom row reveals that the rescaling factor not only affects the degree of high-frequency loss during warping, but also influences the absolute edge strength value of the noise-free approximation $\{\tilde{z}_{t\to 0}^i\}_{i=1}^N$ and the aligned feature $\{\tilde{z}_{t\to 0}^{i,s\times warp \times \frac{1}{s}}\}_{i=1}^N$ Importantly, this relationship is non-monotonic and exhibits a maximum. We attribute this behavior to the fact that different upscaling and downscaling factors alter feature distributions in distinct ways, thereby affecting high-frequency preservation during the denoising process within DM-based pipeline. Furthermore, the location of this optimal point shifts to higher rescaling factors as the super-resolution scale increases. Therefore, to better preserve high-frequency information during DM-based VSR diffusion steps while avoiding excessive computational overhead, we select the rescaling factor s in the rescaling-based warping strategy as 4, 8 and 16 for the $4\times$, $8\times$ and $16\times$ VSR tasks, respectively.

6 COMPARISON OF DGAF-VSR AND MGLD-VSR

MGLD-VSR leverages motion constraints to guide the diffusion process, ensuring temporal consistency. While both methods exploit inter-frame information, our approach is grounded in a quantitative analysis of alignment and compensation between adjacent frames. By enabling effective feature alignment and dense guidance, DGAF-VSR achieves strong temporal consistency while balancing fidelity and perceptual quality without requiring additional temporal modules, unlike MGLD-VSR. Key differences are summarized in Table 2.

- (1) **Warping Procedure.** MGLD-VSR performs warping on low-resolution (LR) features, whereas DGAF-VSR operates on upscaled high-resolution (HR) features, better preserving high-frequency content.
- (2) **Adjacent Information Utilization.** MGLD-VSR incorporates information from adjacent frames only through a motion-guided loss applied after each denoising step. In contrast, DGAF-VSR feeds aligned features directly into both the denoising and guidance U-Nets, enabling more comprehensive exploitation of temporal context.
- (3) **Guiding Source and Strategy.** MGLD-VSR derives guidance exclusively from LR inputs via a U-Net encoder. In contrast, DGAF-VSR receives dense guidance from both LR images and aligned adjacent features through a full U-Net architecture, facilitating richer information integration.
- (4) **Bidirectional Strategy.** MGLD-VSR enforces temporal consistency by constraining forward and backward warping errors during sampling. DGAF-VSR alternates temporal guidance between the previous and next frames at each diffusion step, enabling dynamic and adaptive feature propagation.

7 Experimental Settings

Datasets. We conduct series of experiments on two benchmark synthetic datasets including REDS [35] and Vid4 [4], and a real-world dataset, VideoLQ [10]. For a fair comparison, we adopt the same training set as [8, 6]. The training dataset consists of 296 video sequences from the REDS dataset, with each sequence containing 100 frames and having a standard resolution of 1280 × 720. As for synthetic testing, we utilize four sequences reserved in the REDS dataset ³, which is referred to as the REDS4 dataset, along with the Vid4 dataset. The low-resolution videos in the REDS and Vid4 datasets both undergo 4× bicubic downscaling. For real-world VSR testing, we adopt the testing dataset, VideoLQ, which consists of 50 low-resolution video sequences.

Implementation details. We construct the DGAF-VSR on the pre-trained Stable Diffusion x4 Upscaler model [54, 53], and use pre-trained RAFT [49] to initialize the optical flow estimator introduced in our OGWM module. We utilize DDPM sampling with T=1000 during training and sampling 50 steps during inference. Implemented in PyTorch, the DGAF-VSR is trained on 4 NVIDIA V100 GPUs for around 24 epochs using the Adam optimizer with default parameters (ρ_1 =0.9, ρ_2 =0.999, δ =1 × 10⁻⁸). The training patch size of low-resolution frames is set to 64 × 64 with a 50% probability horizontal flip as data augmentation, and the training batch size is set to 32. The learning rate is fixed to $\delta e - 5$.

Evaluation Metrics. Our assessment employs nine metrics spanning three critical aspects: fidelity, perceptual quality, and temporal consistency. For fidelity evaluation, we utilize standard quantitative measures, including PSNR and SSIM, to assess reconstruction accuracy. The perceptual quality analysis combines two reference-based metrics LPIPS [57] and DISTS [58] with three reference-free metrics MUSIQ [59], CLIP-IQA [60] and NIQE [61] for comprehensive quality assessment. Temporal consistency is evaluated using tLPIPS [52] and tOF [52] across video sequences.

8 QUANTITATIVE COMPARISONS ON DIFFERENT SCALE FACTORS

To validate the adaptability of DGAF-VSR to different scale factors, we compare the VSR performance of various DM-based methods at 8× and 16× scale factors. The experiments are conducted on the REDS4 dataset. As shown in Table 3, our method improves the MUSIQ value by 8.50 and 9.34 over the second-best algorithm for 8× and 16× VSR, respectively. Besides, our network also enhances the CLIP-IQA metric by 24.73% and 46.45% at 8× and 16× scale factors, respectively. This demonstrates that by utilizing a pre-trained 4× Upscaler model along with sufficient alignment and guidance, our DGAF-VSR achieves excellent results in VSR tasks across various scale factors.

³Clips 000, 011, 015, 020 of REDS training set.

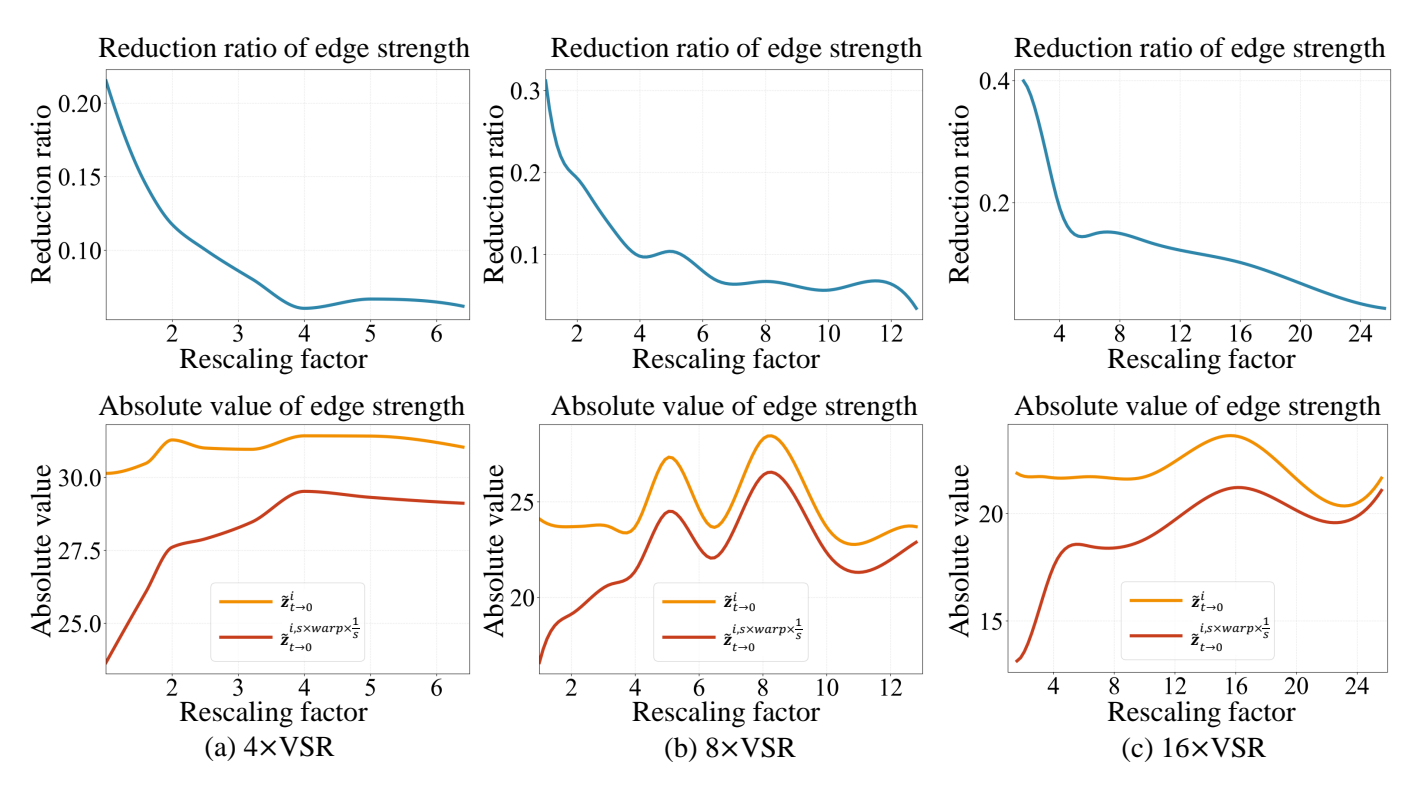


Figure 3: Reduction ratio and absolute edge strength in the rescaling-based warping strategy, as functions of the rescaling factor s. Experiments are conducted on the REDS4 dataset for (a) $4\times$, (b) $8\times$ and (c) $16\times$ VSR task. Reported values are averaged across all diffusion steps and over edge strength computed using three edge detectors: Canny, Sobel, and Laplacian.

Table 2: Comparion of DGAF-VSR and MGLD-VSR.

Method	MGLD-VSR	Ours
Warping Procedure	Low-resolution	High-resolution
Adjacent Information	Motion-guide loss	Aligned features
Bidirectional Strategy	Motion-guided sampling	In-pair guidance strategy
Guiding Source	Image	Image & Feature
Dense Guidance	No	Yes
Quantitative Analysis	No	Yes

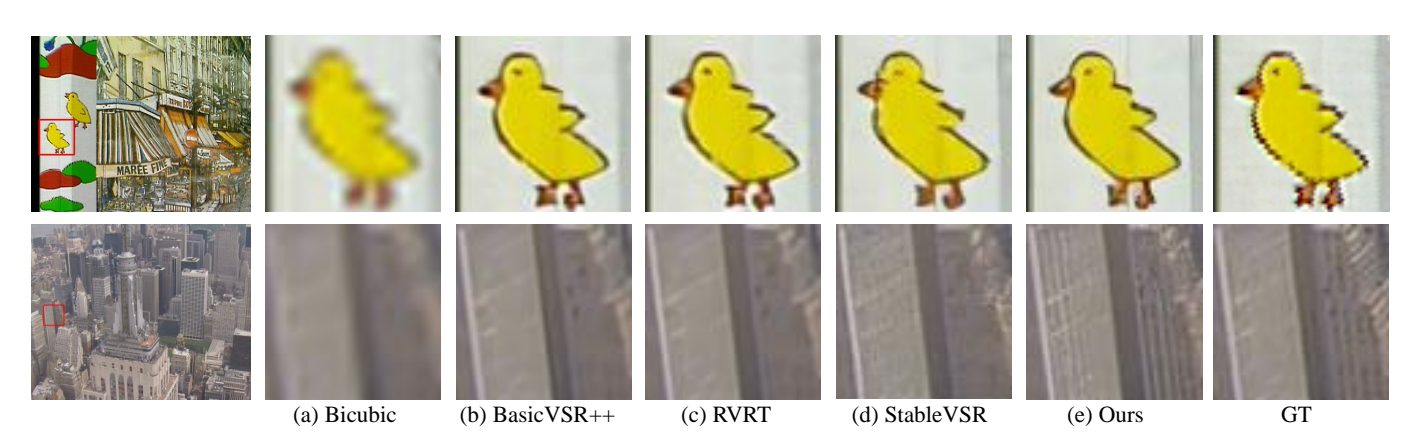


Figure 4: Visualization of the VSR results from different methods on the Vid4 dataset. (a) Bicubic, (b) BasicVSR++, (c) RVRT, (d) StableVSR, (e) Ours.

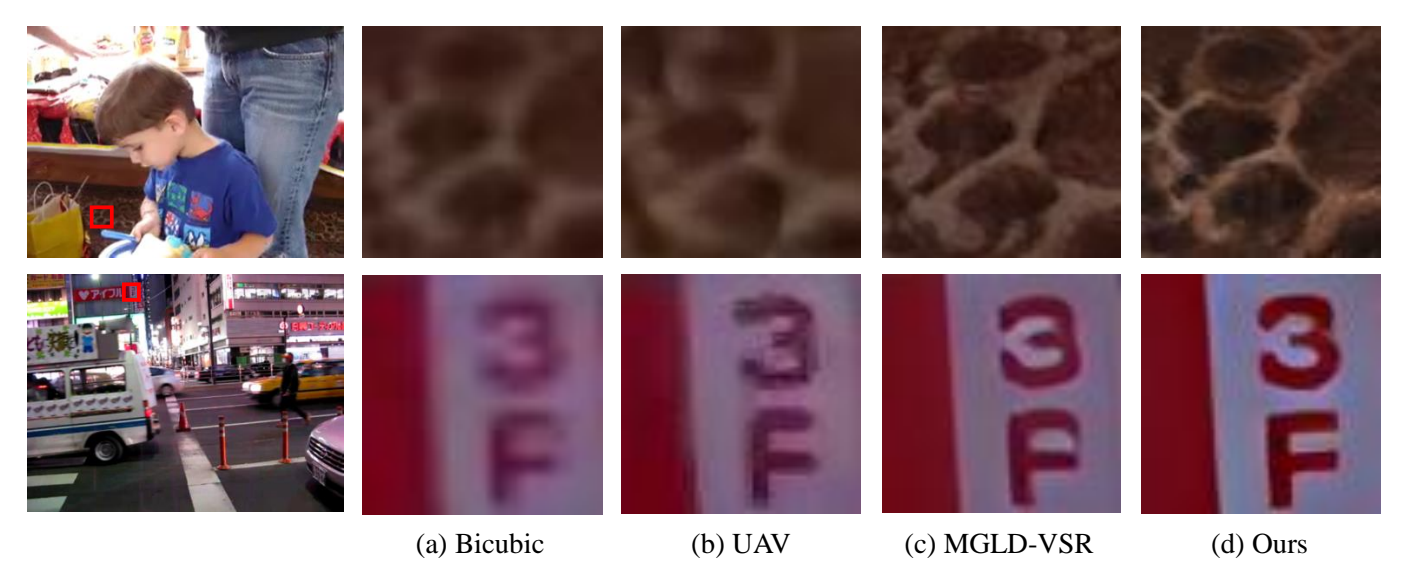


Figure 5: Visualization of the VSR results from different methods on the VideoLQ dataset. (a) Bicubic, (b) UAV, (c) MGLD-VSR, (d) Ours.

Table 3: Quantitative comparison on the REDS4 dataset for $8 \times$ and $16 \times$ VSR, in terms of five perceptual(\diamond) and two fidelity metrics(\star) metrics, with the best results in bold and second bests underlined.

Types	Method	LPIPS⋄↓	DISTS♦↓	MUSIQ⋄↑	CLIP-IQA◊↑	NIQE◊↓	PSNR ⋆ ↑	SSIM⋆↑
	Bicubic	0.688	0.302	21.80	0.372	9.96	21.55	0.588
8×	MGLD-VSR[28]	0.249	0.104	59.44	$\overline{0.271}$	2.86	22.94	0.594
ox	STAR[51]	0.642	$\overline{0.329}$	17.98	0.202	8.08	$\overline{22.23}$	$\overline{0.559}$
	DGAF-VSR	0.224	0.103	67.94	0.464	2.72	23.35	0.601
	Bicubic	0.813	0.403	15.62	0.338	13.17	19.27	0.520
16.	MGLD-VSR[28]	0.381	0.184	58.28	$\overline{0.255}$	2.94	20.49	$\overline{0.494}$
16×	STAR[51]	0.753	0.492	14.12	0.242	10.67	20.26	0.505
	DGAF-VSR	0.343	0.140	67.62	0.495	2.62	21.16	0.537

9 QUALITATIVE COMPARISONS ON THE VID4 DATASET AND THE VIDEOLQ DATASET

Figure 4 visualizes the 4× super-resolution results generated by different methods on the Vid4 dataset. As illustrated in the figure, our DGAF-VSR achieves superior performance in reconstructing fine texture details and structural clarity, particularly in regions such as the beak and edge of the chick, where our method preserves sharpness and natural texture patterns, while competing approaches exhibit blurred edges[9, 6], as well as in the distant building structure, where our approach maintains distinct architectural features without introducing unrealistic artifacts observed in DM-based methods like StableVSR[13].

Figure 5 visualizes the 4× super-resolution results generated by different methods on the real-world VideoLQ dataset. As illustrated, compared to other DM-based VSR approaches, our DGAF-VSR achieves superior performance in edge reconstruction and the generation of fine-grained, colorful details. This advantage is particularly evident in regions such as the patterns on the carpet and the shape of the letter 'F', where competing methods produce blurred contours and implausible structural artifacts [12, 28].

10 High-frequency preservation of DGAF-VSR

According to observation 2, performing warping operations on upscaled features has the potential to mitigate the high-frequency loss commonly observed during the warping process. Additionally, the subsequent downscaling of these warped features is capable of counteracting the high-frequency loss introduced by the upscaling operation. This dual mechanism serves as the cornerstone of the design of our Optical Guided Warping Module (OGWM). To validate this concept experimentally, we visualize the edge and high-pass components of three feature representations $\tilde{z}_{1\to 0}^i$, $\tilde{z}_{1\to 0}^{i,warp}$ and $\tilde{z}_{1\to 0}^{i,s\times warp\times \frac{1}{s}}$ in Figure. 6. As is evident from the figure, the high-frequency components of $\tilde{z}_{1 \to 0}^{i,warp}$ exhibit significant detail loss and edge blurring compared to the original feature $\tilde{z}_{1\to 0}^i$. In contrast, the high-frequency components of $z_{1\rightarrow 0}^{i,s\times warp \times \frac{1}{s}}$ are nearly identical to those of $\tilde{z}_{1\to 0}^i$. These experimental results provide compelling evidence supporting the effectiveness of the proposed OGWM module, demonstrating that DGAF-VSR significantly improves the retention of high-frequency information during the warping process.

11 Efficiency of DGAF-VSR

To evaluate the efficiency of our network, we compare the peak GPU memory of DGAF-VSR with that of SOTA DM-based VSR methods. The peak GPU memory consumption is recorded on an NVIDIA V100-32G GPU at an output resolution of 720p (720×1280). As shown in Table 4, the peak GPU memory of our DGAF-VSR is 14.96% and 51.11% lower than that of StableVSR and STAR, respectively, indicating the efficiency of our network.

In terms of runtime, we evaluate the performance of different modules using an NVIDIA V100-32G GPU on the REDS4 dataset. As shown in Table 5, the upscaling and downscaling

Table 4: Comparion of the peak GPU memory overhead, with the lowest consumption in bold.

Method	MGLD-VSR	StableVSR	STAR	Ours
Memory (GB)	25.61	14.04	24.42	11.94

processes contribute only 2.51% and 1.73% to the total runtime of the OGWM, respectively. Notably, for each diffusion step, the average runtime of the OGWM module and the FTCM module are 2.43 e-5 and 0.4505 seconds, respectively. The FM module incurs an overhead of 0.3178 seconds for each frame, accounting for only 1.32% of the total inference runtime.

Furthermore, we provide the number of parameters in Table 6. As shown, the proposed DGAF-VSR contains 983.3 MB of network parameters, with 473 MB being trainable. The number of parameters in DGAF-VSR is significantly smaller than that of MGLD-VSR (1465 MB) and STAR (2139 MB).

12 Ablation study

Effect of the in-pair guidance strategy. The purpose of the in-pair forward and backward guidance strategy is to alternately integrate the aligned information from the forward and backward frames with the information from the current frame. Therefore, validating the effectiveness of this strategy is essential. As shown in Table 7, a comparison between Case 1 and Case 5 evaluates the 4× VSR performance with and without the in-pair forward and backward guidance strategy. As shown, incorporating this strategy improves PSNR by 0.29 dB and reduces the tLPIPS value by 20.65%, indicating significant improvements in fidelity, perceptual quality, and temporal consistency. These results substantiate the effectiveness of the in-pair guidance strategy.

Effect of the pre-upscaling strategy. In the flow predicting module (FM), input frames are pre-upscaled to serve as inputs for the RAFT-based optical flow estimator. In this ablation study, we validate the effectiveness of this strategy. Comparing the results of Case 2 and Case 5 in Table 7, we observe that the pre-upscaling strategy leads to a 1.26 dB improvement in PSNR, an 18.80% reduction in LPIPS, and a 14.24% reduction in tOF. This indicates that the pre-upscaling strategy can achieve better VSR performance.

Effect of the optical flow estimator. The proposed DGAF-VSR utilizes a RAFT-based optical flow estimator. To verify the effectiveness of the estimator, we compare the VSR results obtained using different optical flow estimators. Comparing Case 5 with Case 3 and Case 4 in Table 7, it can be observed that adopting the RAFT-based optical flow estimator yields a PSNR improvement of 0.89 dB and 0.13 dB over the Farneback and SpyNet estimators, respectively. Additionally, the temporal consistency metric tLPIPS also shows improvements of 51.66% and 11.31% compared to Farneback and SpyNet. Therefore, we select RAFT as the optical flow estimator for DGAF-VSR.

Effect of the rescaling factor. Table 8 presents the 4× VSR performance of our proposed DGAF-VSR under different rescaling factors in the rescaling-based warping strategy of OGWM. As shown, DGAF-VSR achieves the best perceptual

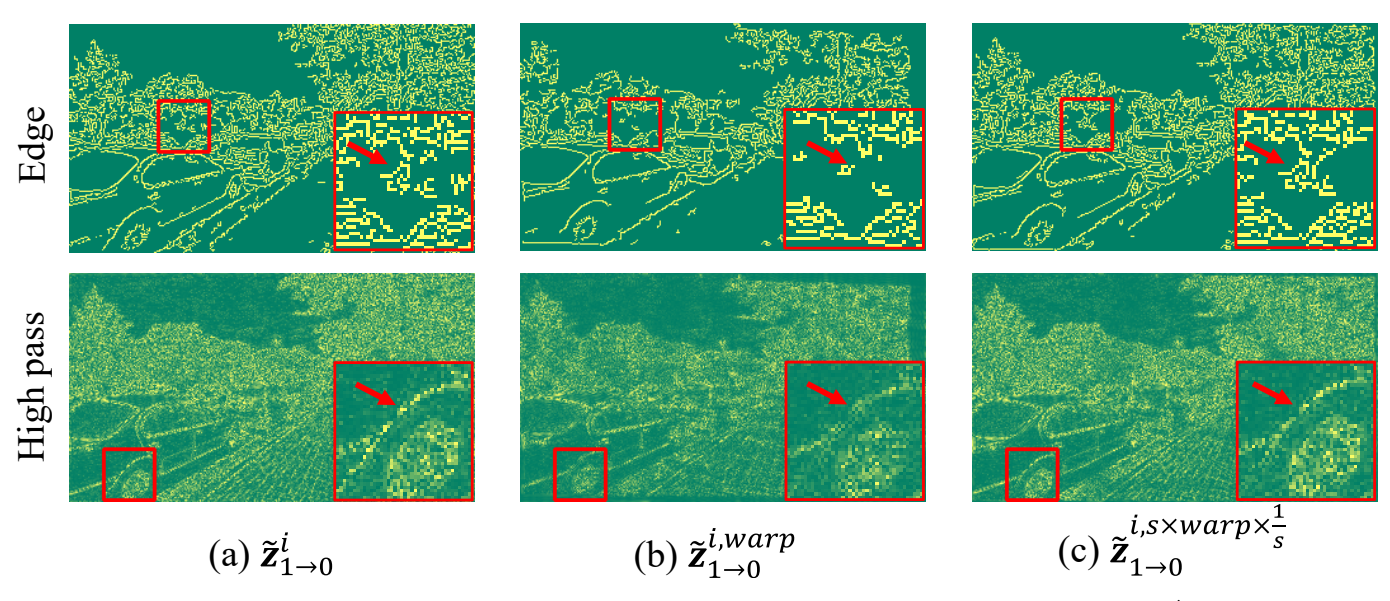


Figure 6: Visualization of the edge and high-pass component of (a) the original features $\tilde{z}_{1\to 0}^i$, (b) the features $\tilde{z}_{1\to 0}^{i,warp}$ warped on the original size, and (c) the features $\tilde{z}_{1\to 0}^{i,s\times warp\times \frac{1}{s}}$ obtained through rescaling-based warping strategy.

Table 5: Runtime per frame of different modules in our proposed DGAF-VSR.

		Eac	ch diffusio							
	OGWM					Total	FM	VAE decoder	Total(steps=50)	
	upscaling	downscaling	Warping	Total	FTCM	Total				
Runtime(s)	6.11 e-7	4.21 e-7	2.33 e-5	2.43 e-5	0.4504	0.4504	0.3178	1.3137	24.15	

Table 6: The number of parammeters of different modules.

	FM	F	ГСМ	VAE	Total	Trainable	
	LIVI	Guiding UNet	Denoising UNet	VAE	Total	Tramable	
Trainable	No	Yes	No	No	-	-	
Pamameters(M)	5.3	473	473	32	983.3	473	

Table 7: The effects of the in-pair guidance strategy, the pre-upscaling strategy and the choice of optical flow estimator, in terms of two fidelity (\star) , two perceptual (\diamond) and two temporal consistency (\circ) metrics, with the best results in bold.

Case	In-pair guidance	Pre/Post Upscaling	Optical flow	PSNR⋆↑	SSIM⋆↑	LPIPS♦↓	DISTS≎↓	tLPIPS∘↓	tOF∘↓
1		Pre	RAFT	27.88	0.796	0.097	0.043	4.94	2.74
2	✓	Post	RAFT	26.91	0.765	0.117	0.051	14.06	3.16
3	✓	Pre	SpyNet	28.04	0.801	0.101	0.045	4.42	2.76
4	✓	Pre	Farneback	27.28	0.774	0.116	0.053	8.11	2.96
5(Ours)	✓	Pre	RAFT	28.17	0.804	0.095	0.043	3.92	2.71

quality, temporal consistency, and fidelity on the REDS4 dataset when the rescaling factor s=4. This result aligns well with Observation 2 in our manuscript.

13 Limitations and Future Work

Our proposed framework introduces an effective alignment mechanism for high-frequency preservation and a novel compensation approach for enhanced information integration, both of which are potentially beneficial for various low-level vision tasks. DGAF-VSR is built upon the pre-trained Stable Diffusion ×4 Upscaler, a backbone commonly adopted by existing diffusion-based VSR methods [12, 13, 62]. Consequently, while our method achieves state-of-the-art performance on 4x, 8x, and 16× VSR tasks, it shares the same limitation as prior works: when applied to other low-level video restoration tasks, such as denoising or deblurring, its performance may degrade due to the scale-specific design of the diffusion model. Nevertheless, we argue that by implementing simple, task-oriented modifications like LoRA, any general-purpose T2I diffusion model (e.g., SD-XL [63] and SDv3.5 [64]) can serve as our foundational model. This inherent flexibility implies that the advancements introduced by our DGAF-VSR are readily transferable to diverse video reconstruction tasks, such as video denoising and video deblurring. We leave this promising extension for future research but emphasize its potential significance for advancing general video restoration frameworks.

1	DDEDDINE	DETHINKING	DIEFLICION	Moder P	LOED V	IDEA CI	IDED D	COLUTION:	LEVED CINC	Device (THIDANCE EDOM	ALTONIED.	Er ATIBEC	O

Table 8: Effect of the rescaling factor on the $4 \times VSR$ task over the REDS4 dataset, in terms of two fidelity (\star), two perceptual (\diamond) and two temporal consistency (\circ) metrics, with the best results in bold.

Rescaling factor	PSNR ⋆ ↑	SSIM⋆↑	LPIPS◊↓	DISTS♦↓	tLPIPS∘↓	tOF∘↓
1.0	27.22	0.768	0.114	0.054	12.03	2.99
1.6	26.89	0.761	0.113	0.051	17.05	3.04
2.0	28.01	0.798	0.098	0.045	4.78	2.82
2.5	27.39	0.780	0.105	0.047	12.0	2.89
3.2	27.50	0.782	0.104	0.047	10.19	2.80
4.0 (Ours)	28.17	0.804	0.095	0.045	3.92	2.71
5.0	28.16	0.804	0.095	0.046	3.93	2.77
6.4	27.59	0.785	0.103	0.047	9.76	2.84